Journal of Alloys and Compounds 671 (2016) 74–83

Contents lists available at ScienceDirect

Journal of Alloys and Compounds

journal homepage: http://www.elsevier.com/locate/jalcom

Electrochemical properties of CuO hollow nanopowders prepared from formless Cu–C composite via nanoscale Kirkendall diffusion process

Jong Min Won [a], Jong Hwa Kim [b], Yun Ju Choi [c], Jung Sang Cho [a], Yun Chan Kang [a, *]

[a] Department of Materials Science and Engineering, Korea University, Anam-Dong, Seongbuk-Gu, Seoul 136-713, Republic of Korea
[b] Daegu Center, Korea Basic Science Institute, 80 Daehakro Bukgu, Daegu 702-701, Republic of Korea
[c] Suncheon Center, Korea Basic Science Institute, Suncheon 540-742, Republic of Korea

ARTICLE INFO

Article history:
Received 9 October 2015
Received in revised form
30 January 2016
Accepted 30 January 2016
Available online 3 February 2016

Keywords:
Kirkendall diffusion
Copper oxide
Anode material
Lithium-ion battery
Spray drying

ABSTRACT

Hollow CuO nanopowders are prepared using a simple spray drying process that relied on nanoscale Kirkendall diffusion; these nanopowders have potential applications in lithium-ion batteries. Citric acid is used as both the carbon source material and chelating agent and plays a key role in the preparation of the hollow nanopowders. The formless Cu–C composite that formed as an intermediate product transforms into slightly aggregated CuO hollow nanopowders after post-treatment at 300 and 400 °C under an air atmosphere. The CuO hollow nanopowders exhibit higher initial discharge capacities and better cycling performances than those of the filled-structured CuO nanopowders, which are prepared at a post-treatment temperature of 500 °C under an air atmosphere. The discharge capacities of the CuO nanopowders post-treated at 300, 400, and 500 °C for the 150th cycle at a current density of 1 A g^{-1} are 793, 632, and 464 mA h g^{-1}, respectively, and their capacity retentions calculated from the maximum discharge capacities are 88, 80, and 73%, respectively. The CuO nanopowders with hollow structures exhibit better structural stability for repeated lithium insertion and desertion processes than those with filled structures.

1. Introduction

Nanostructured transition metal oxides have been studied as anode materials for lithium-ion batteries (LIBs) for several decades [1–15]. The detailed structure and mean size of the nanostructured materials strongly affect the electrochemical properties of transition metal oxides for lithium-ion storage. Therefore, various types of liquid-solution and gas-phase reaction processes have been applied for the preparation of transition metal oxide materials for LIBs [16–27]. Nanostructured cupric oxide (CuO) materials, which have the advantages of low cost, chemical stability, and nontoxicity and exhibit various nanobelt, nanofiber, necklace, and bundle-like morphologies, have also been studied as anode materials for LIBs [28–50]. In particular, Zhou et al. reported the preparation of copper oxide hollow nanoparticles/graphene-nanosheet composites by applying the Kirkendall effect [50]. The difference between the rates of the outward diffusion of metal cations through the oxide layer and the inward diffusion of oxygen ions into the metals during the oxidation process creates hollow-structured metal oxide nanopowder [51–53].

Spray drying is one of the most preferred commercial processes for the preparation of dry powders from a liquid solution or slurry [54,55]. Thus far, several reports have demonstrated the use of spray drying for the preparation of nanostructured spherical materials for applications in LIBs [56–62]. However, to the best of our knowledge, the preparation of cupric oxide hollow nanopowders by spray drying of an aqueous spray solution containing metal salts has not been reported.

* Corresponding author.
E-mail address: yckang@korea.ac.kr (Y.C. Kang).

http://dx.doi.org/10.1016/j.jallcom.2016.01.252
0925-8388/

Herein, we attempted to synthesize hollow CuO nanopowders using a simple spray drying process applying nanoscale Kirkendall diffusion. The precursor powders, which were several tens of micrometers in size, prepared by the spray drying process transformed into several hundred CuO hollow nanopowders after a two-step post-treatment process. Citric acid, which was used as both the carbon source material and chelating agent, played a key role in the preparation of the slightly aggregated CuO hollow nanopowders. The morphological and electrochemical properties of the CuO nanopowders post-treated at various temperatures were investigated.

2. Experimental

The CuO hollow nanopowders were prepared using a commercial spray drying system followed by a two-step post-treatment process. The precursor spray solutions were obtained by dissolving pre-determined quantities of copper nitrate trihydrate [$Cu(NO_3)_2 \cdot 3H_2O$, Samchun] and citric acid (as a chelating agent) in distilled water. The concentration of copper nitrate trihydrate was fixed at 0.1 M. Similarly, the concentration of the citric acid used as a carbon source material and chelating agent was maintained at 0.1 M. The temperatures at the inlet and outlet of the spray dryer were 300 °C and 120 °C, respectively. A two-fluid nozzle was used as an atomizer, and the atomization pressure was 0.5 bar. To produce CuO hollow nanopowders, the precursor powders obtained by the spray drying process were post-treated at 400 °C in a 10% H_2/Ar gas mixture for 3 h and subsequently held at temperatures of 300, 400, and 500 °C in air for 3 h.

The crystal structures of the powders were investigated using X-ray diffractometry (XRD, X'Pert PRO MPD) with Cu-Kα radiation (λ = 1.5418 Å) at the Korea Basic Science Institute (Daegu). The morphologies of the powders were investigated using field-emission scanning electron microscopy (FE-SEM, Hitachi S-4800) and high-resolution transmission electron microscopy (HR-TEM, JEOL JEM-2100F) at a working voltage of 200 kV. The specific surface areas of the powders were calculated based on Brunauer–Emmett–Teller (BET) analysis of nitrogen-adsorption measurements (TriStar 3000).

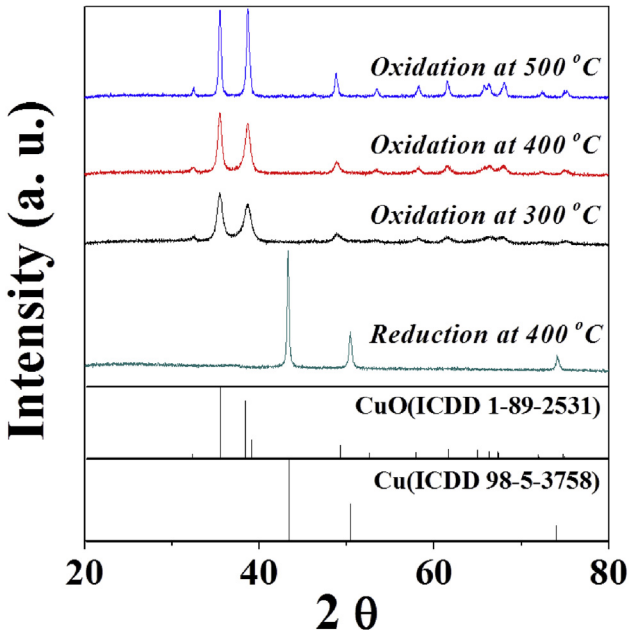

Fig. 1. XRD patterns of the Cu–C and CuO nanopowders prepared by the first and second step of the post-treatment process.

The electrochemical properties of the powders were analyzed by constructing a 2032-type coin cell. The anode was prepared by mixing the active material, carbon black, and sodium carboxymethyl cellulose (CMC) in a weight ratio of 7:2:1. Li metal and microporous polypropylene film were used as the counter electrode and separator, respectively. The dimensions of the negative electrode were 1 cm × 1 cm, and the active mass loading of the active materials was approximately 1.0 mg cm^{-2}. The electrolyte

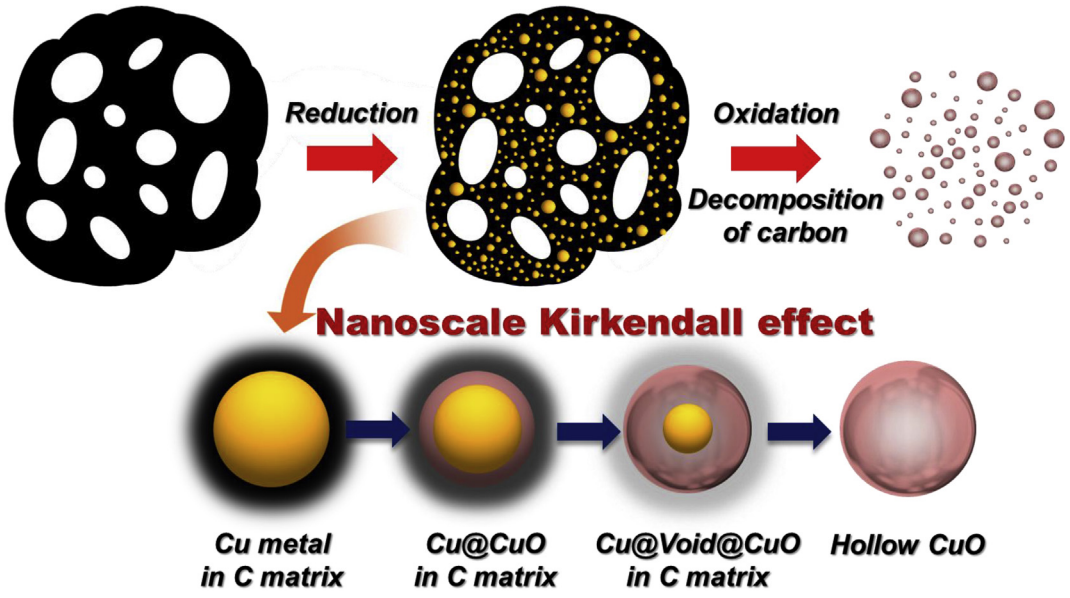

Scheme 1. Schematic diagram of the formation mechanism of the hollow CuO nanopowders produced via the nanoscale Kirkendall diffusion process.

was 1 M $LiPF_6$ dissolved in a mixture of fluoroethylene carbonate/dimethyl carbonate (FEC/DMC; 1:1 v/v). The discharge/charge characteristics of the samples were investigated by cycling in the 0.001–3 V potential range at various current densities. Cyclic voltammograms were measured at a scan rate of 0.07 mV s^{-1}. Electrochemical impedance spectra were obtained by AC electrochemical impedance spectroscopy (EIS) with a ZIVE SP1 over a frequency range of 0.01 Hz–100 kHz and at the potential amplitude of 10 mV.

3. Results and discussion

The transformation of one copper–citrate–nitrate complex powder prepared by the spray drying process into numerous hollow CuO nanopowders via nanoscale Kirkendall diffusion is described in Scheme 1. The first step, decomposition of the copper–citrate–nitrate complex under a H_2/Ar atmosphere, produced the Cu–C composite, in which Cu nanopowders were uniformly embedded within the porous carbon matrix. One CuO hollow nanopowder was formed from one Cu nanopowder by the nanoscale Kirkendall diffusion process during the second step of the post-treatment under air atmosphere. Complete combustion of the carbon matrix occurred during the post-treatment process. Consequently, the Cu–C composite transformed into several hundred carbon-free CuO hollow nanopowders with slight aggregation between the nanopowders.

The crystal structure and morphology of the Cu–C composite prepared by the first step of the post-treatment process under a reducing atmosphere are shown in Figs. 1 and 2, respectively. The XRD pattern in Fig. 1 shows the complete conversion of copper–citrate–nitrate into metallic copper. The spherical morphology of the precursor powders directly obtained by the spray-drying process transformed into the formless structure after the first step of the post-treatment process, as observed in the SEM and TEM images in Fig. 2. Fast decomposition of the copper–citrate–nitrate precursor and evolution of a large amount of combustion gas during the post-treatment process resulted in the formless structure. The SEM and TEM images in Fig. 2b–d reveal ultrafine Cu nanopowders uniformly dispersed all over the semitransparent carbon matrix. The high-resolution TEM image in Fig. 2e reveals clear lattice fringes separated by 0.25 nm, which corresponds to the (111) crystal plane of metallic Cu. Segregation of metallic Cu occurred during the reduction process, resulting in Cu nanopowders with a broad size distribution. The mean size and geometric standard deviation of the Cu nanopowders measured from the TEM images were 62 nm and 1.72, respectively. The TG curve of the Cu–C composite powders is shown in Fig. S1. A strict weight increase was observed in the TG curve from 155 °C owing to the oxidation of Cu metal into CuO. A weight loss was observed from 300 °C onward owing to the degradation of amorphous carbon. The carbon content of the Cu–C composite estimated from the TG analysis was 14.5 wt %.

The Cu–C composite transformed into the carbon-free CuO powders during the second step of the post-treatment process at temperatures of 300, 400, and 500 °C under an air atmosphere. The XRD patterns in Fig. 1 reveal the complete conversion of metallic Cu into CuO, irrespective of the post-treatment

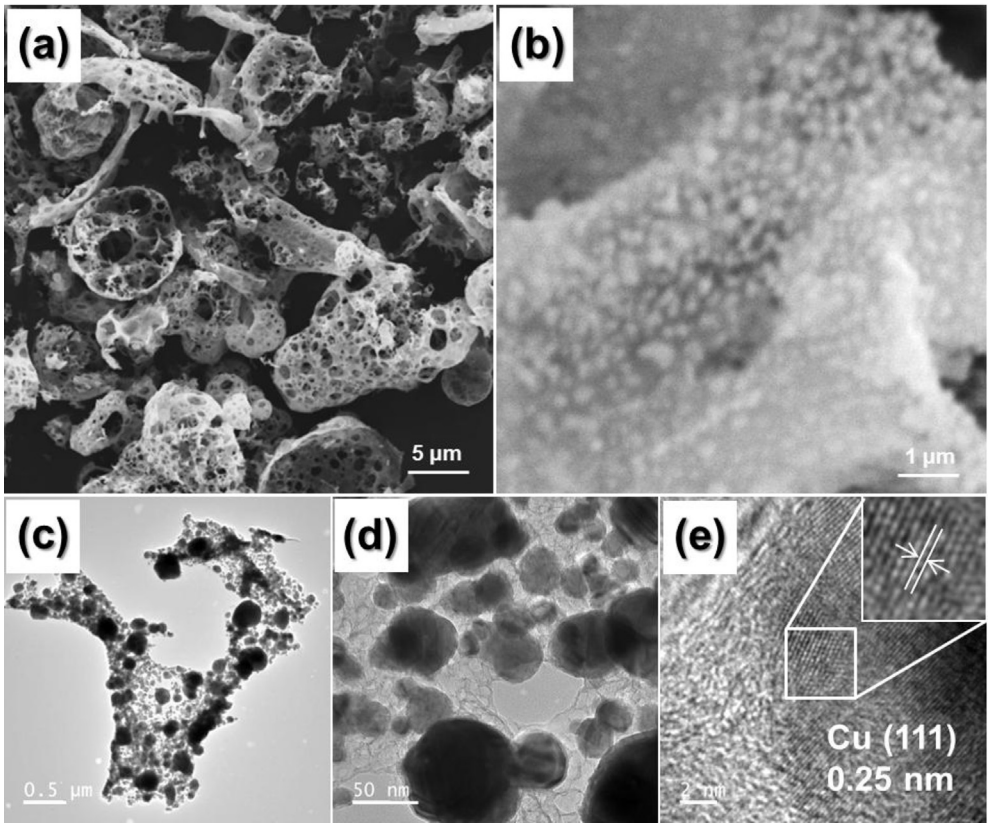

Fig. 2. Morphologies of the Cu–C composite prepared by the first step of the post-treatment process under a reducing atmosphere.

temperature. The mean crystallite sizes of the CuO powders obtained at the post-treatment temperatures of 300, 400, and 500 °C calculated from the (111) peak widths of the XRD patterns using the Scherrer equation were 13, 17, and 26 nm, respectively. The existence of metallic Cu within the CuO nanopowders post-treated at various temperatures under air atmosphere was studied by XPS analysis as shown in Fig. S2. The Cu 2p spectra of the CuO nanopowders show only Cu peaks for the oxide, with binding energies of CuO (933.1 eV for Cu $2p_{3/2}$ and 953.0 eV for Cu $2p_{1/2}$). The peaks for metallic Cu were not observed in the XPS spectra. The results of XPS analysis confirmed the formation of pure CuO powders without metallic Cu by post-treatment process even at a temperature of 300 °C.

The formless structure of the Cu–C composite was maintained after the second step of the post-treatment process at 300 °C, as observed in Fig. 3a. However, the CuO nanopowders observed in the TEM images in Fig. 3b and c exhibit different morphologies compared with those of the Cu nanopowders. The dense-structured Cu nanopowders transformed into hollow-structured CuO nanopowders via the well-known nanoscale Kirkendall diffusion process [51–53]. A dense-structured Cu@CuO nanopowder with a core–shell structure was first formed by surface oxidation of the Cu nanopowder. In addition, the small-radius Cu (Cu^{2+} = 73 pm) cation diffused outward more rapidly than the inward diffusion of oxygen anions (O^{2-} = 140 pm). The volume of empty voids and the size of the nanopowder increased upon increasing the post-treatment time. Consequently, complete diffusion out of Cu cations resulted in a hollow CuO nanopowder as a result of the nanoscale Kirkendall diffusion process. The shell thickness of the CuO nanopowder observed in the TEM image in Fig. 3c was 14 nm. The high-resolution TEM image in Fig. 3d reveals clear lattice fringes separated by 0.23 nm, which corresponds to the (111) crystal plane of CuO. The morphologies of the nanopowders obtained after post-treatment process for 5 min at a temperature of 300 °C are shown in Fig. S3 to confirm the formation mechanism of the hollow CuO nanopowders. The Cu@CuO nanopowders with core–shell structure and the Cu@void@CuO nanopowders with yolk-shell structure formed as intermediate products were observed in the TEM images. The morphologies of the CuO nanopowders obtained at a post-treatment temperature of 400 °C are shown in Fig. 4. The SEM and TEM images of the unground powders obtained directly by post-treatment in Fig. 4a–c reveal an aggregated structure between the

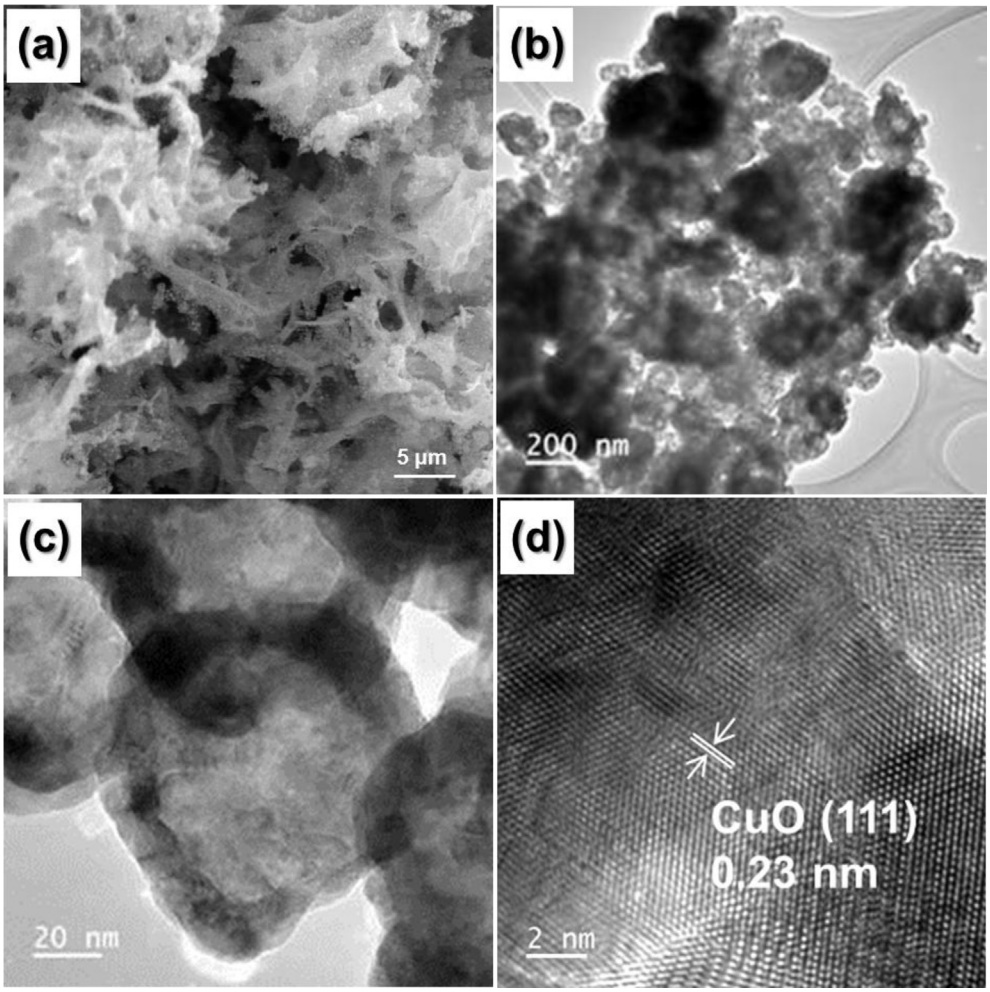

Fig. 3. Morphologies of the hollow CuO nanopowders prepared by the second step of the post-treatment process at 300 °C under air atmosphere: (a) SEM image, (b) and (c) TEM images, and (d) high resolution TEM image.

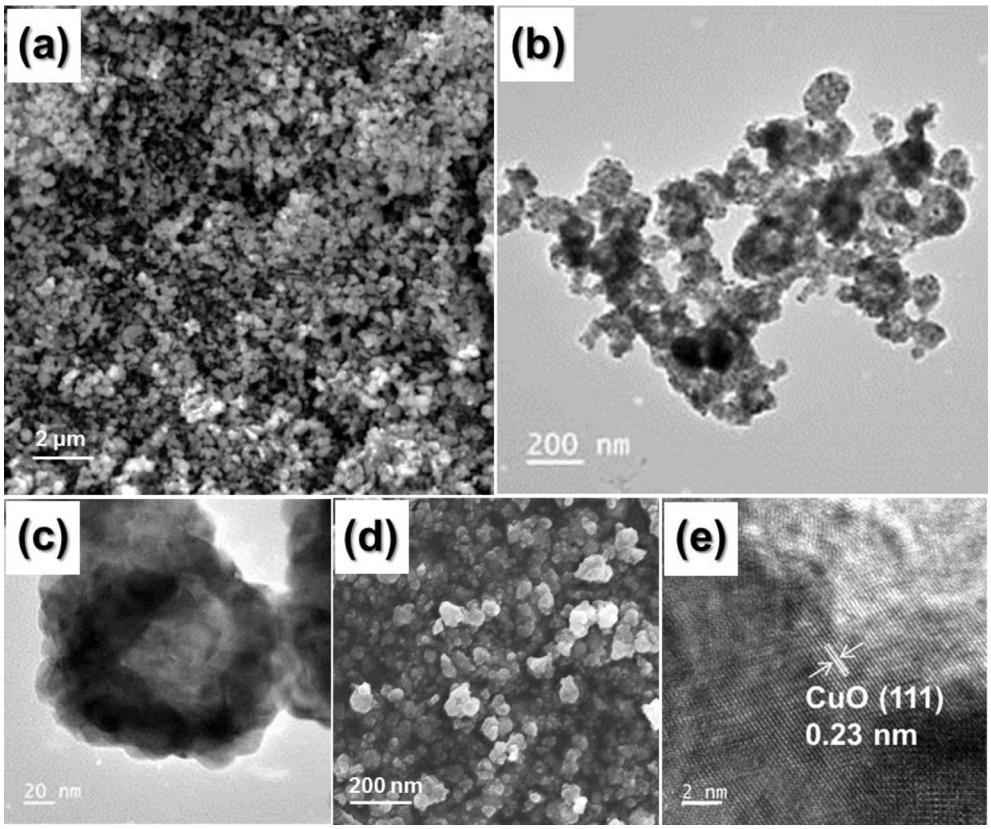

Fig. 4. Morphologies of the hollow CuO nanopowders prepared by the second step of the post-treatment process at 400 °C under air atmosphere: (a) SEM image, (b) and (c) TEM images, (d) SEM image obtained after milling process, and (e) high resolution TEM image.

nanopowders. Necking between the nanopowders occurred during the nanoscale Kirkendall diffusion process after combustion of the carbon material, acting as a barrier for the aggregation of the nanopowders. However, the field-emission SEM (FE-SEM) image in Fig. 4d reveals the aggregation-free CuO nanopowders obtained after simple hand milling using an agate mortar. The high-resolution TEM images in Fig. 4b and c reveal the clear hollow structure of the CuO nanopowders. The shell thickness of the CuO nanopowder observed in the TEM image in Fig. 4c was 28 nm. The shell thickness of the CuO nanopowders increased upon increasing the post-treatment temperature under an air atmosphere in the sintering process, as observed in Figs. 3c and 4c. The high-resolution TEM image in Fig. 4e reveals the crystalline structure of the CuO nanopowders formed by the nanoscale Kirkendall diffusion process. The morphologies of the CuO nanopowders obtained at a high post-treatment temperature of 500 °C are shown in Fig. 5. The formless Cu–C material transformed into the CuO nanopowders with slight aggregation between the nanopowders even without the milling process, as observed in the SEM image in Fig. 5a. The TEM image in Fig. 5b shows the filled structure of the CuO nanopowders. Some of the large-size CuO nanopowders had hollow inner structures with large shell thicknesses, as observed in the TEM image in Fig. 5c. The hollow CuO nanopowders formed by the nanoscale Kirkendall diffusion process transformed into filled CuO nanopowders as a result of the sintering process. The elemental mapping images in Fig. S4 show the formation of carbon-free CuO nanopowders irrespective of the post-treatment temperatures under air atmosphere. The thermogravimetric (TG) curves in Fig. S5 also show the complete combustion of the carbon material during the second step of the post-treatment process under an air atmosphere. The BET surface areas of the CuO nanopowders post-treated at temperatures of 300, 400, and 500 °C were 12, 12, and 18 $m^2\ g^{-1}$, respectively.

The electrochemical properties of the CuO nanopowders prepared at different second-step post-treatment temperatures are shown in Figs. 6 and 7. The cyclic voltammogram (CV) curves of the three samples performed at a scanning rate of 0.07 mV s^{-1} are shown in Fig. 6. In the first cathodic sweep, the three samples exhibited clear reduction peaks at approximately 1.18 and 0.8 V, which are related to the complete reduction of Cu^{2+} to Cu^{+} by the formation of the Cu_2O phase and decomposition of Cu_2O into Cu and Li_2O, respectively [63,64]. The reduction peak observed at approximately 0.8 V is also related to the growth of solid electrolyte interphase (SEI) layers over the powders [63,64]. The broad reduction peak observed over 1.3 V in Fig. 6a and b was attributed to the formation of Li_xCuO and $Cu^{II}_{1-x}Cu^{I}_{x}O_{1-x/2}$ [65]. In the anodic sweep, the broad oxidation peak observed at approximately 2.4 V was attributed to the formation of Cu_2O ($Cu^0 + Li_2O \leftrightarrow Cu_2O + Li_2O$) as well as the partial oxidation of Cu_2O into CuO [65]. The charge and discharge curves of the three samples for the 1st cycle at a constant current density of 1 A g^{-1} are presented in Fig. 6d. The CuO nanopowders prepared at post-treatment temperatures of 300 and

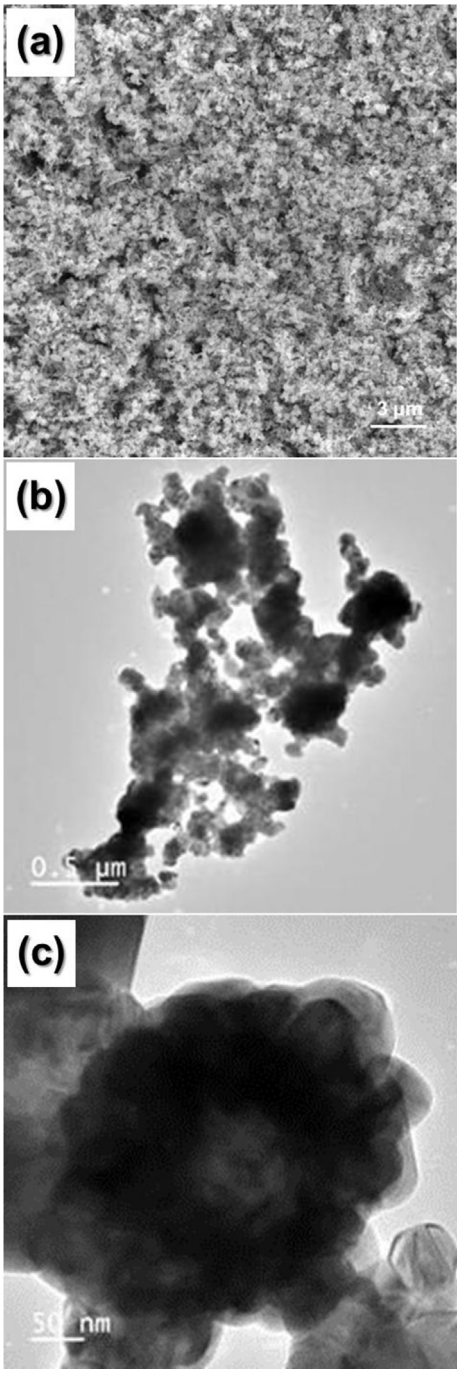

Fig. 5. Morphologies of the CuO nanopowders prepared by the second step of the post-treatment process at 500 °C under air atmosphere: (a) SEM image, (b) and (c) TEM images.

400 °C had three plateaus in their first discharge curves at approximately 1.75, 1.3, and 0.9 V. The initial discharge capacities of the powders post-treated at 300, 400, and 500 °C were 1134, 1079, and 1011 mA h g^{-1}, respectively, and their corresponding charge capacities were 797, 617, and 463 mA h g^{-1}, respectively. The theoretical capacity of CuO as anode material for lithium ion battery is ca. 670 mA h g^{-1}. The extra capacity of the CuO nanopowders may be due to the partial reversible formation and decomposition of the gel-like SEI film on the surface of the electrode and pseudo capacitance [66].

The cycling performances of the CuO nanopowders prepared at different second-step post-treatment temperatures at a constant current density of 1 A g^{-1} are shown in Fig. 7a. The discharge capacities of the powders post-treated at 300, 400, and 500 °C for the 2nd cycle were 832, 628, and 473 mA h g^{-1}, respectively, and their discharge capacities for the 10th cycles were 896, 786, and 623 mA h g^{-1}, respectively. The discharge capacities of the three samples gradually increased from the 2nd to 10th cycle. The kinetically activated electrolyte degradation and the formation of a polymeric gel-like film on the surface of the nanopowders in the low potential region increased the specific capacities during the first 10 cycles [67]. The Coulombic efficiencies for the three samples are shown in Fig. S6. The initial Coulombic efficiencies of the CuO nanopowders obtained at the post-treatment temperatures of 300, 400, and 500 °C were 70.3%, 57.2%, and 45.8%, respectively. The CuO nanopowders obtained at the high post-treatment temperatures of 500 °C had low initial Coulombic efficiency due to their poor structural stability during lithium insertion and desertion processes. The three samples had high Coulombic efficiencies over 100% due to the step-by-step activation of metallic Cu located inside the hollow CuO nanopowders during the first 10 cycles. The discharge capacities of the powders post-treated at 300, 400, and 500 °C for the 150th cycle were 793, 632, and 464 mA h g^{-1}, respectively, and their capacity retentions calculated from the maximum discharge capacities were 88, 80, and 73%, respectively. The different morphologies and mean crystallite sizes of the CuO nanopowders post-treated at 300, 400, and 500 °C affected their initial discharge and charge capacities and cycling performances. The rate performance of the hollow CuO nanopowders post-treated at 300 °C is shown in Fig. 7b, in which the current density was increased step-wise from 0.2 to 3 A g^{-1}. The hollow CuO nanopowders had final discharge capacities of 999, 918, 827, 763, 723, 683, 658, and 614 mA h g^{-1} at current densities of 0.2, 0.4, 0.6, 0.8, 1.0, 1.5, 2.0, and 3.0 A g^{-1}, respectively. The discharge capacities of the hollow CuO nanopowders were well recovered to 883 mA h g^{-1} when the current density was returned to 0.2 A g^{-1} after cycling at high current densities. Electrochemical impedance spectroscopy of the CuO nanopowders post-treated at 300 and 500 °C before and after cycling was conducted to evaluate their electrochemical properties. The resulting Nyquist plots presented in Fig. 7c, d, and S7 contain semicircles in the medium-frequency range, which are assigned to the charge-transfer resistance (R_{ct}) of the electrodes [68,69]. Fig. 7e shows the equivalent circuit model used for ac impedance fitting. The CuO nanopowders post-treated at 500 °C show the largest R_{ct} of 201.8 Ω before cycling, as shown in Fig. S7a. The charge-transfer resistances of the three samples decreased after the first cycling because of the transformation of the crystalline structure into an amorphous structure after the first cycle. The R_{ct} of the nanopowders increased from 8.1 to 10.4 Ω for the CuO post-treated at 300 °C, from 17.8 to 19.5 Ω for the CuO post-treated at 400 °C, and from 19.1 to 43.5 Ω for the CuO post-treated at 500 °C as the number of cycles increases from 1st to 10th cycle, as shown in Fig. 7c and d. The hollow CuO nanopowders post-treated at 300 and 400 °C maintained their low charge-transfer resistances during the first 10 cycles. However, the charge-transfer resistances of the filled CuO nanopowders post-treated at 500 °C increased during cycling. In particular, the R_{ct} of the CuO nanopowders post-treated at 300 and 400 °C for the 50th cycle were almost the same. However, the R_{ct} of CuO nanopowders post-treated at 500 °C increased

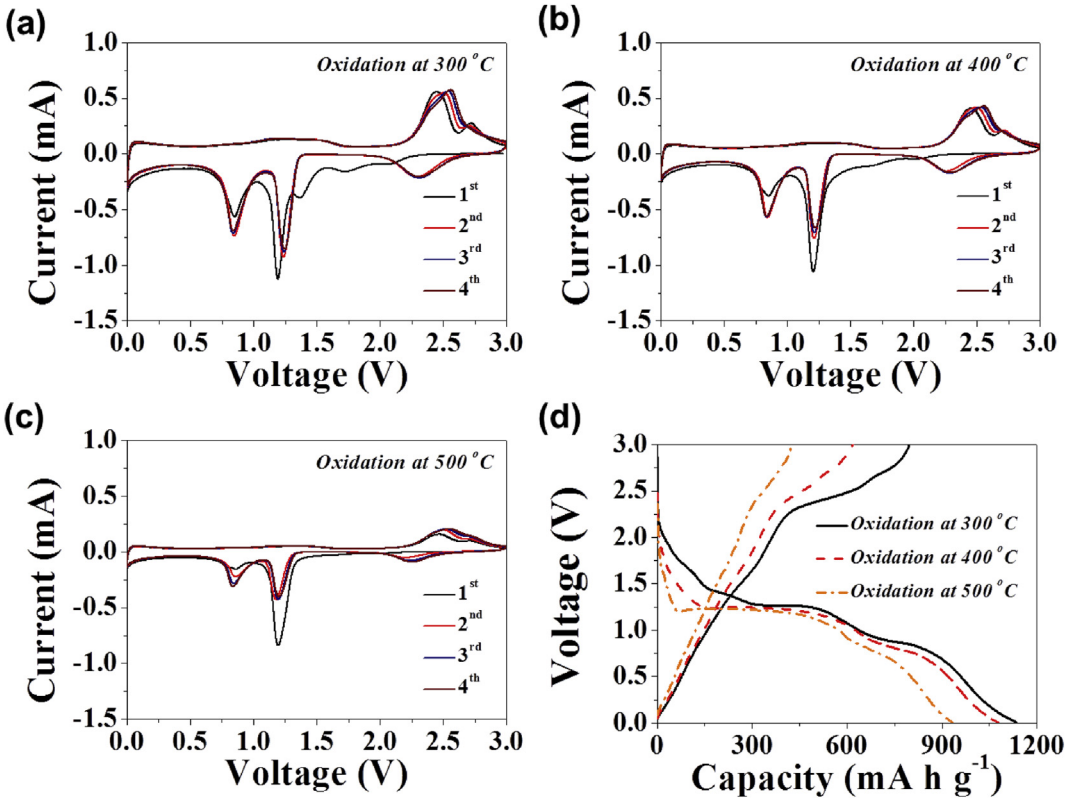

Fig. 6. Electrochemical properties of the CuO nanopowders prepared by the second step of the post-treatment process at various temperatures: CV curves of the powders obtained at (a) 300 °C, (b) 400 °C, (c) 500 °C, and (d) initial charge/discharge curves.

largely from 43.5 to 201.3 Ω during the further 40 cycles, as shown in Fig. S7b. The structural destruction of the CuO nanopowders post-treated at 500 °C during repeated lithium insertion and desertion processes increased the charge-transfer resistances during cycling. On the other hand, the CuO nanopowders post-treated at 300 and 400 °C had high structural stability during repeated lithium insertion and desertion processes due to their accommodation of large volume changes during cycling. The morphologies of the CuO nanopowders obtained after 50 cycles are shown in Fig. S8. The hollow structure of the CuO nanopowders prepared by the second step of the post-treatment process at 300 °C under air atmosphere was maintained even after 50 cycles. On the other hand, the spherical morphology of the CuO nanopowders prepared by the second step of the post-treatment process at 500 °C under air atmosphere was destroyed after 50 cycles. The CuO nanopowders with hollow structures exhibited better structural stability for repeated lithium insertion and desertion processes than those with filled structures. The electrochemical properties of the CuO hollow nanopowders are compared with those of the CuO materials with various morphologies reported in the previous literatures, and the results are summarized in Table S1. The carbon-coated CuO hollow powders prepared by spray pyrolysis had a discharge capacity of 750 mA h g^{-1} at a current density of 670 mA g^{-1} after 300 cycles [63]. Graphene-supported shuttle- and urchin-like CuO had a discharge capacity of 826 mA h g^{-1} at a current density of 700 mA g^{-1} after 100 cycles [70]. However, the prepared CuO hollow nanopowders had superior electrochemical properties compared to those of the bare CuO materials reported in the previous literatures.

4. Conclusions

The spray-drying process was applied in the large-scale production of CuO hollow nanopowders. The spherical Cu-citrate-nitrate powder obtained by the spray-drying process transformed into a formless Cu–C composite after post-treatment under a reducing atmosphere. The formless Cu–C composite produced numerous CuO hollow nanopowders via the nanoscale Kirkendall diffusion process. The amorphous carbon formed from citric acid minimized the aggregation of Cu and CuO nanopowders during the second step of the post-treatment process. The different morphologies and mean crystallite sizes of the CuO nanopowders post-treated at various temperatures affected their initial discharge and charge capacities and cycling performances. The mean crystallite sizes of the CuO powders obtained at the post-treatment temperatures of 300, 400, and 500 °C were 13, 17, and 26 nm, respectively. The optimum post-treatment temperature for the nanoscale Kirkendall diffusion process to prepare CuO hollow nanopowders exhibiting good electrochemical properties for lithium-ion storage was 300 °C. This simple spray-drying process applying nanoscale Kirkendall diffusion could be widely applied in the preparation of transition metal oxide hollow nanopowders for wide applications including energy storage.

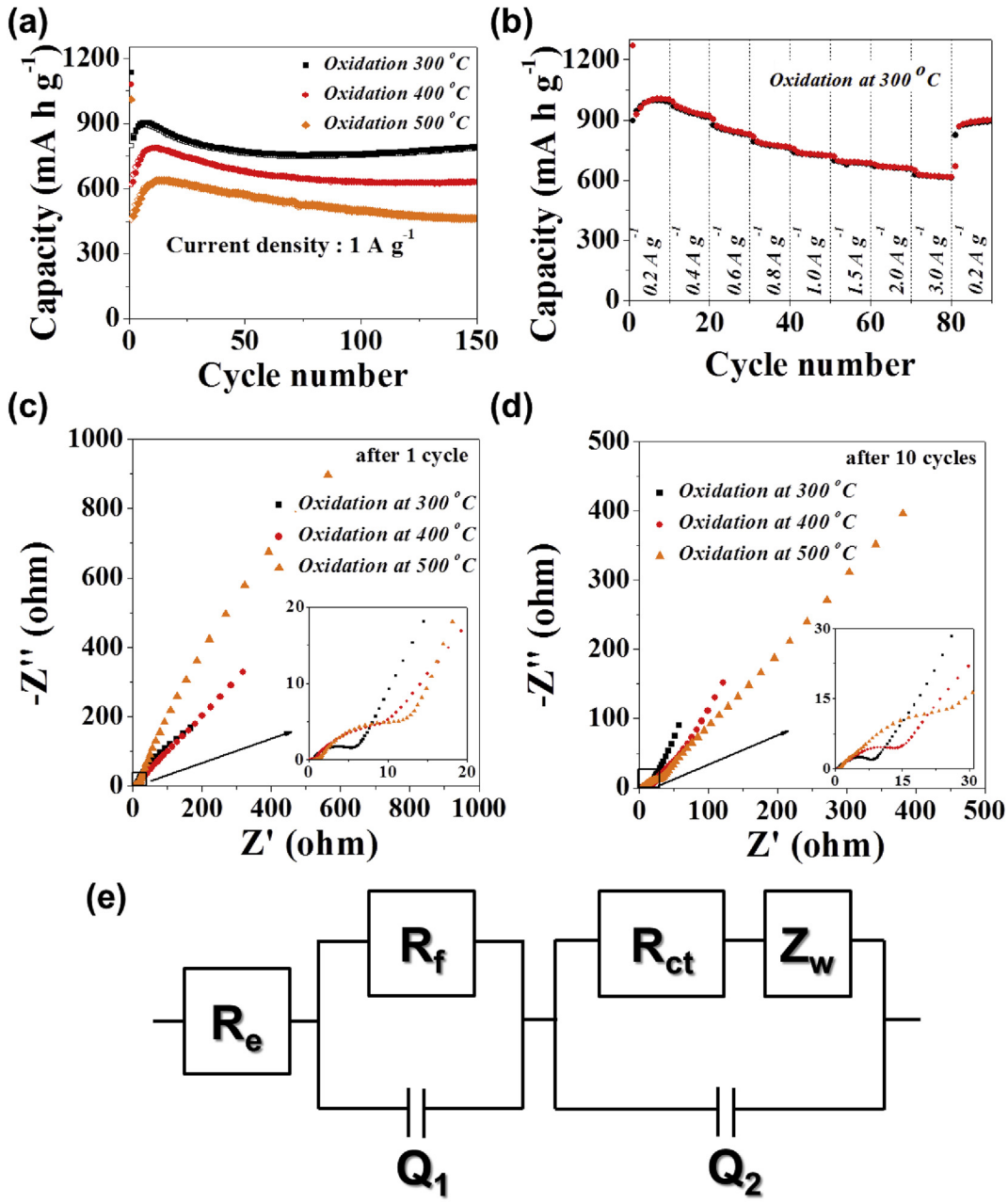

Fig. 7. Electrochemical properties of the CuO nanopowders prepared by the second step of the post-treatment process at various temperatures: (a) cycling performances, (b) rate performance, (c) Nyquist plots after 1st cycle, and (d) Nyquist plots after 10th cycle, (e) Equivalent electrical circuit.

Acknowledgment

This work was supported by a National Research Foundation of Korea (NRF) grant funded by the Korea government (MEST) (NRF-2015R1A2A1A15056049).

Appendix A. Supplementary data

Supplementary data related to this article can be found at http://dx.doi.org/10.1016/j.jallcom.2016.01.252.

References

[1] P. Poizot, S. Laruelle, S. Grugeon, L. Dupont, J.M. Tarascon, Nano-sized transition-metal oxides as negative-electrode materials for lithium-ion batteries, Nature 47 (2000) 496–499.
[2] Q. Qu, T. Gao, H. Zheng, X. Li, H. Liu, M. Shen, J. Shao, Graphene oxides-guided growth of ultrafine Co_3O_4 nanocrystallites from MOFs as high-performance anode of Li-ion batteries, Carbon 92 (2015) 119–125.
[3] M.V. Reddy, G.V.S. Rao, B.V.R. Chowdari, Metal oxides and oxysalts as anode materials for Li ion batteries, Chem. Rev. 113 (2013) 5364–5457.
[4] J. Kong, X. Yao, Y. Wei, C. Zhao, J.M. Anga, X. Lu, Polydopamine-derived porous nanofibers as host of $ZnFe_2O_4$ nanoneedles: towards high-performance anodes for lithium-ion batteries, RSC Adv. 5 (2015) 13315–13323.
[5] L. Zhang, H.B. Wu, X.W. Lou, Iron-oxide-based advanced anode materials for lithium-ion batteries, Adv. Energy Mater. 4 (2014) 1300958.
[6] J.S. Chen, X.W. Lou, SnO_2-based nanomaterials: synthesis and application in lithium-ion batteries, Small 9 (2013) 1877–1893.
[7] J.S. Cho, Y.J. Hong, Y.C. Kang, Design and synthesis of bubble-nanorod-structured Fe_2O_3–carbon nanofibers as advanced anode material for Li-ion batteries, ACS Nano 9 (2015) 4026–4035.
[8] X. Lu, R. Wang, Y. Bai, J. Chen, J. Sun, Facile preparation of a three-dimensional

Fe_3O_4/macroporous graphene composite for high-performance Li storage, J. Mater. Chem. A 3 (2015) 12031–12037.
[9] Y.Z. Jiang, D. Zhang, Y. Li, T.Z. Yuan, N.F. Bahlawane, C. Liang, W.P. Sun, Y.H. Lu, M. Yan, Amorphous Fe_2O_3 as a high-capacity, high-rate and long-life anode material for lithium ion batteries, Nano Energy 4 (2014) 23–30.
[10] G. Zhang, X.W. Lou, General synthesis of multi-shelled mixed metal oxide hollow spheres with superior lithium storage properties, Angew. Chem. Int. Ed. 126 (2014) 9187–9190.
[11] F. Han, W.C. Li, C. Lei, B. He, K.C. Oshida, A.H. Lu, Selective formation of carbon-coated, metastable amorphous $ZnSnO_3$ nanocubes containing mesopores for use as high-capacity lithium-ion battery, Small 10 (2014) 2637–2644.
[12] S.M. Xu, C.M. Hessel, H. Ren, R. Yu, Q. Jin, M. Yang, H.J. Zhao, D. Wang, α-Fe_2O_3 multi-shelled hollow microspheres for lithium ion battery anodes with superior capacity and charge retention, Energy Environ. Sci. 7 (2014) 632–637.
[13] J. Wang, N. Yang, H. Tang, Z. Dong, Q. Jin, M. Yang, D. Kisailus, H.J. Zhao, Z.Y. Tang, D. Wang, Accurate control of multishelled Co_3O_4 hollow microspheres as high-performance anode materials in lithium-ion batteries, Angew. Chem. Int. Ed. 52 (2013) 6417–6420.
[14] Z. Zhu, F. Cheng, J. Chen, Investigation of effects of carbon coating on the electrochemical performance of $Li_4Ti_5O_{12}$/C nanocomposites, J. Mater. Chem. A 1 (2013) 9484–9490.
[15] C. Liu, F. Li, L.P. Ma, H.M. Cheng, Advanced materials for energy storage, Adv. Mater. 22 (2010) E28–E62.
[16] X.W. Lou, C.M. Li, L.A. Archer, Designed synthesis of coaxial SnO_2@carbon hollow nanospheres for highly reversible lithium storage, Adv. Mater. 21 (2009) 2536–2539.
[17] C.K. Chan, X.F. Zhang, Y. Cui, High capacity Li ion battery anodes using Ge nanowires, Nano Lett. 8 (2008) 307–309.
[18] M. Srivastava, J. Singh, T. Kuila, R.K. Layek, N.H. Kim, J.H. Lee, Recent advances in graphene and its metal-oxide hybrid nanostructures for lithium-ion batteries, Nanoscale 7 (2015) 4820–4868.
[19] S.M. Yuan, J.X. Li, L.T. Yang, L.W. Su, L. Liu, Z. Zhou, Preparation and lithium storage performances of mesoporous Fe_3O_4@C microcapsules, ACS Appl. Mater. Interfaces 3 (2011) 705–709.
[20] L. Wang, W. Tang, Y. Jing, L. Su, Z. Zhou, Do transition metal carbonates have greater lithium storage capability than oxides? A case study of monodisperse $CoCO_3$ and CoO microspindles, ACS, Appl. Mater. Interfaces 6 (2014) 12346–12352.
[21] J.B. Wu, R.Q. Guo, X.H. Huang, Y. Lin, Ternary core/shell structure of Co_3O_4/NiO/C nanowire arrays as high-performance anode material for Li-ion battery, J. Power Sources 248 (2014) 115–121.
[22] J. Chen, X.H. Xia, J.P. Tu, Q.Q. Xiong, Y.X. Yu, X.L. Wang, C.D. Gu, Co_3O_4–C core–shell nanowire array as an advanced anode material for lithium ion batteries, J. Mater. Chem. 22 (2012) 15056–15061.
[23] H. Jiang, Y. Hu, S. Guo, C. Yan, P.S. Lee, C. Li, Rational design of MnO/Carbon nanopeapods with internal void space for high-rate and long-life Li-ion batteries, ACS Nano 8 (2014) 6038–6046.
[24] S.H. Choi, Y.C. Kang, Crumpled graphene–molybdenum oxide composite powders: preparation and application in lithium-ion batteries, ChemSusChem 7 (2014) 523–528.
[25] Y. Shi, J.Z. Wang, S.L. Chou, D. Wexler, H.J. Li, K. Ozawa, H.K. Liu, Y. Wu, Hollow structured Li_3VO_4 wrapped with graphene nanosheets in situ prepared by a one-pot template-free method as an anode for lithium-ion batteries, Nano Lett. 13 (2013) 4715–4720.
[26] B. Wang, J.L. Cheng, Y. Wu, D. Wang, D.N. He, Porous NiO fibers prepared by electrospinning as high performance anode materials for lithium ion batteries, Electrochem. Commun. 23 (2012) 5–8.
[27] Y. Shi, J. Gao, H.D. Abruna, H.J. Li, H.K. Liu, D.W., J.Z. Wang, Y. Wu, The Mechanism of the One-Step Synthesis of Hollow-Structured Li_3VO_4 as an anode for lithium-ion batteries, Chem. Eur. J. 20 (2014) 5608–5612.
[28] Y.J. Hong, Y.C. Kang, Superior electrochemical performances of double-shelled CuO yolk–shell powders formed from spherical copper nitrate–polyvinylpyrrolidone composite powders, RSC Adv. 4 (2014) 58231–58237.
[29] R. Sahay, P.S. Kumar, V. Aravindan, J. Sundaramurthy, W.C. Ling, S.G. Mhaisalkar, S. Ramakrishna, S. Madhavi, High aspect ratio electrospun CuO nanofibers as anode material for lithium-ion batteries with superior cycleability, J. Phys. Chem. C 116 (2012) 18087–18092.
[30] Y. Zhang, M. Xu, F. Wang, X. Song, Y. Wang, S. Yang, CuO necklace: controlled synthesis of a metal oxide and carbon nanotube heterostructure for enhanced lithium storage performance, J. Phys. Chem. C 117 (2013) 12346–12351.
[31] L.L. Wang, W. Cheng, H. Gong, C. Wang, D. Wang, K. Tang, Y. Qian, Facile synthesis of nanocrystalline-assembled bundle-like CuO nanostructure with high rate capacities and enhanced cycling stability as an anode material for lithium-ion batteries, J. Mater. Chem. 22 (2012) 11297–11302.
[32] M.V. Reddy, C. Yu, F. Jiahuan, K.P. Loh, B.V.R. Chowdari, Li-cycling properties of molten salt method prepared nano/submicrometer and micrometer-sized CuO for lithium batteries, ACS Appl. Mater. Interfaces 5 (2013) 4361–4366.
[33] C. Wang, Q. Li, F.F. Wang, G.F. Xia, R.Q. Liu, D. Li, N. Li, J.S. Spendelow, G. Wu, Morphology-dependent performance of CuO anodes via facile and controllable synthesis for lithium-ion batteries, ACS Appl. Mater. Interfaces 6 (2014) 1243–1250.
[34] J. Wang, Y.C. Liu, S. Wang, X.T. Guo, Y.P. Liu, Facile fabrication of pompon-like hierarchical CuO hollow microspheres for high-performance lithium-ion batteries, J. Mater. Chem. A 2 (2014) 1224–1229.
[35] B. Wang, X.L. Wu, C.Y. Shu, Y.G. Guo, C.R. Wang, Synthesis of CuO/graphene nanocomposite as a high-performance anode material for lithium-ion batteries, J. Mater. Chem. 20 (2010) 10661–10664.
[36] Y.M. Zhang, W.X. Zhang, M. Li, Z. Yang, G. Chen, Q. Wang, Cosurfactant-mediated microemulsion to free-standing hierarchical CuO arrays on copper substrates as anodes for lithium-ion batteries, J. Mater. Chem. A 1 (2013) 14368–14374.
[37] J.H. Ju, K.S. Ryu, Synthesis and performance of CuO with complex hollow structure as anode material for lithium secondary batteries, J. Electrochem. Soc. 158 (2011) A814–A817.
[38] F. Cheng, J. Liang, Z. Tao, J. Chen, Functional materials for rechargeable batteries, Adv. Mater. 23 (2011) 1695–1715.
[39] S.W. Ko, J.I. Lee, H.S. Yang, S.J. Park, U.Y. Jeong, Mesoporous CuO particles threaded with CNTs for high-performance lithium-ion battery anodes, Adv. Mater. 24 (2012) 4451–4456.
[40] M.A. Dar, S.H. Nam, Y.S. Kim, W.B. Kim, Synthesis, characterization, and electrochemical properties of self-assembled leaf-like CuO nanostructures, J. Solid State Electrochem. 14 (2010) 1719–1726.
[41] M. Xu, F. Wang, B. Ding, X. Song, J. Fang, Electrochemical synthesis of leaf-like CuO mesocrystals and their lithium storage properties, RSC Adv. 2 (2012) 2240–2243.
[42] Q. Zhang, D. Xu, X. Zhou, X. Wu, K. Zhang, In situ synthesis of CuO and Cu nanostructures with promising electrochemical and wettability properties, Small 10 (2014) 935–943.
[43] R. Wu, X. Qian, F. Yu, H. Liu, K. Zhou, J. Wei, Y. Huang, MOF-templated formation of porous CuO hollow octahedra for lithium-ion battery anode materials, J. Mater. Chem. A 1 (2013) 11126–11129.
[44] J. Wang, Q. Zhang, X. Li, D. Xu, Z. Wang, H. Guo, K. Zhang, Three-dimensional hierarchical Co_3O_4/CuO nanowire heterostructure arrays on nickel foam for high-performance lithium ion batteries, Nano Energy 6 (2014) 19–26.
[45] L. Wang, H. Gong, C. Wang, D. Wang, K. Tang, Y. Qianab, Facile synthesis of novel tunable highly porous CuO nanorods for high rate lithium battery anodes with realized long cycle life and high reversible capacity, Nanoscale 4 (2012) 6850–6855.
[46] Q. Yu, H. Huang, R. Chen, P. Wang, H.S. Yang, M.X. Gao, X.S. Peng, Z. Yea, Synthesis of CuO nanowalnuts and nanoribbons from aqueous solution and their catalytic and electrochemical properties, Nanoscale 4 (2012) 2613–2620.
[47] C.S. Choi, Y.U. Park, H. Kim, N.R. Kim, K. Kang, H.M. Lee, Three-dimensional sponge-like architectured cupric oxides as high-power and long-life anode material for lithium rechargeable batteries, Electrochim. Acta 70 (2012) 98–104.
[48] X. Wang, D.M. Tang, H. Li, W. Yi, T. Zhai, Y. Bando, D. Golberg, Revealing the conversion mechanism of CuO nanowires during lithiation–delithiation by in situ transmission electron microscopy, Chem. Commun. 48 (2012) 4812–4814.
[49] Z. Wang, F. Su, S. Madhavi, X.W. Lou, CuO nanostructures supported on Cu substrate as integrated electrodes for highly reversible lithium storage, Nanoscale 3 (2011) 1618–1623.
[50] J. Zhou, L. Ma, H. Song, B. Wu, X. Chen, Durable high-rate performance of CuO hollow nanoparticles/graphene-nanosheet composite anode material for lithium-ion batteries, Electrochem. Commun. 13 (2011) 1357–1360.
[51] Y. Yin, R.M. Rioux, C.K. Erdonmez, S. Hughes, G.A. Somorjai, A.P. Alivisatos, Durable high-rate performance of CuO hollow nanoparticles/graphene-nanosheet composite anode material for lithium-ion batteries, Science 304 (2004) 711–714.
[52] X.W. Lou, L.A. Archer, Z. Yang, Hollow micro-/nanostructures: synthesis and applications, Adv. Mater. 20 (2008) 3987–4019.
[53] Z. Wang, L. Zhou, X.W. Lou, Metal oxide hollow nanostructures for lithium-ion batteries, Adv. Mater. 24 (2012) 1903–1911.
[54] K. Okuyama, M. Abdullah, I.W. Lenggoro, F. Iskandar, Preparation of functional nanostructured particles by spray drying, Adv. Powder Technol. 17 (2006) 587–611.
[55] A.B.D. Nandiyanto, K. Okuyama, Progress in developing spray-drying methods for the production of controlled morphology particles: from the nanometer to submicrometer size ranges, Adv. Powder Technol. 22 (2011) 1–19.
[56] D.S. Jung, T.H. Hwang, S.B. Park, J.W. Choi, Spray drying method for large-scale and high-performance silicon negative electrodes in Li-ion batteries, Nano Lett. 13 (2013) 2092–2097.
[57] J.H. Kim, Y.C. Kang, Electrochemical properties of micron-sized, spherical, meso- and macro-porous Co_3O_4 and CoO–carbon composite powders prepared by a two-step spray drying process, Nanoscale 6 (2014) 4789–4795.
[58] G.W. Zhou, J. Wang, P. Gao, X. Yang, Y.S. He, X.Z. Liao, J. Yang, Z.F. Ma, Facile spray drying route for the three-dimensional graphene-encapsulated Fe_2O_3 nanoparticles for lithium ion battery anodes, Ind. Eng. Chem. Res. 52 (2013) 1197–1204.
[59] G.D. Park, J.H. Kim, Y.J. Choi, Y.C. Kang, Large-scale production of MoO_3-reduced graphene oxide powders with superior lithium storage properties by spray-drying process, Electrochim. Acta 173 (2015) 581–587.
[60] F. Gao, Z. Tang, J. Xue, Preparation and characterization of nano-particle $LiFePO_4$ and $LiFePO_4$/C by spray-drying and post-annealing method, Electrochim. Acta 53 (2007) 1939–1944.
[61] J.M. Won, S.H. Choi, Y.J. Hong, Y.N. Ko, Y.C. Kang, Electrochemical properties of yolk-shell structured $ZnFe_2O_4$ powders prepared by a simple spray drying

process as anode material for lithium-ion battery, Sci. Rep. 4 (2014) 5857.
[62] G.D. Park, Y.C. Kang, Superior lithium-ion storage properties of mesoporous CuO–reduced graphene oxide composite powder prepared by a two-step spray-drying process, Chem. Eur. J. 21 (2015) 9179–9184.
[63] Y.H. Xu, G.Q. Jian, M.R. Zachariah, C.S. Wang, Nano-structured carbon-coated CuO hollow spheres as stable and high rate anodes for lithium-ion batteries, J. Mater. Chem. A 1 (2013) 15486–15490.
[64] K. Chen, D.F. Xue, Room-temperature chemical transformation route to CuO nanowires toward high-performance electrode materials, J. Phys. Chem. C 117 (2013) 22576–22583.
[65] A. Débart, Z.L. Dupont, P. Poizot, J.B. Leriche, J.M. Tarascon, A transmission electron microscopy study of the reactivity mechanism of tailor-made CuO particles toward lithium, J. Electrochem. Soc. 148 (2001) A1266–A1274.
[66] Y. Zhu, N. Sun, W. Lin, Y. Ma, C. Lai, Q. Wang, Facile fabrication of three-dimensional hierarchical CuO nanostructures with enhanced lithium storage capability, RSC Adv. 5 (2015) 68061–68066.
[67] S. He, J. Li, J. Wang, G. Yang, Z. Qiao, Facile synthesis and lithium storage performance of hollow CuO microspheres, Mater. Lett. 129 (2014) 5–7.
[68] C.C. Fu, G.S. Li, D. Luo, J. Zheng, L.P. Li, Gel-combustion synthesis of $Li_{1.2}Mn_{0.4}Co_{0.4}O_2$ composites with a high capacity and superior rate capability for lithium-ion batteries, J. Mater. Chem. A 2 (2014) 1471–1483.
[69] N.R. Srinivasan, S. Mitra, R. Bandyopadhyaya, Improved electrochemical performance of SnO_2–mesoporous carbon hybrid as a negative electrode for lithium ion battery applications, Phys. Chem. Chem. Phys. 16 (2014) 6630–6640.
[70] L.Q. Lu, Y. Wang, Facile synthesis of graphene-supported shuttle-and urchin-like CuO for high and fast Li-ion storage, Electrochem. Commun. 14 (2012) 82–85.